Interplay between Collective and Localized Effects of Point Defects on Photoelectrochemical Performance of TiO_2 Photoanodes for Oxygen Evolution

*Mengya Yang, Junyi Cui, Matyas Daboczi, Robert V. Law, Joel Luke, Ji-Seon Kim, Anna Hankin, and Salvador Eslava**

Among the various photoanode materials investigated for photoelectrochemical water splitting cells, TiO_2 stands out due to its abundance, stability, and favorable valence band edge for water oxidation. In this study, the importance of introducing and combining oxygen and titanium vacancy point defects in anatase TiO_2 photoanodes to improve their performance is unveiled, achieving a photocurrent density of 0.73 (±0.015) mA cm^{-2} at +1.23 V_{RHE} under 100 mW cm^{-2} of simulated sunlight or 26.4 mA cm^{-2} at +1.23 V_{RHE} under 100 mW cm^{-2} of 365 nm light. The characterization by X-ray photoelectron spectroscopy, surface photovoltage, and electron paramagnetic resonance demonstrates that these oxygen and titanium vacancies can have both collective and localized positive effects on the material, leading to a narrowing of the bandgap, an increase in donor density, and an increase in hydroxyl groups on the surface of TiO_2. These result in enhanced light absorption, conductivity, and photovoltage, as well as a more negative flat-band potential and increase in hole flux to the semiconductor–electrolyte interface. These findings provide valuable insights into the role of point defects in modulating the properties of TiO_2 and have important implications for the development of high-performance TiO_2-based devices.

1. Introduction

Photoanodes play a critical role in photoelectrochemical (PEC) water splitting, which is a promising technology for producing sustainable and clean hydrogen fuel. Suitable n-type semiconductors are required to construct photoanodes and generate holes under illumination to efficiently oxidize water.[1] Among the various n-type semiconductors, titanium dioxide (TiO_2) has gained substantial attention due to its low cost, high chemical stability, and excellent photo-corrosion resistance.[2–4] Different phases of TiO_2, such as rutile, anatase, and brookite, have been extensively studied, but typically anatase shows superior performance due to lower charge carrier recombination and higher adsorption strength of hydroxyl groups. We recently developed an aerosol-assisted chemical vapor deposition (AACVD) of $Ti_{16}O_{16}(OEt)_{32}$ clusters that leads to a nanostructured anatase TiO_2 with exposed {0 1 0} facets. The morphology of this TiO_2 resembles the crystals of gypsum, sand and water found in nature, also known as desert roses.[5] This TiO_2 achieves high incident photon-to-current efficiency (IPCE) close to 100% at 1.23 V versus the reversible hydrogen electrode (V_{RHE}). This high IPCE is, however, achieved at 350 nm due to the TiO_2 bandgap of 3.2 eV, which limits the wide spectral utilization of solar light. Therefore, it is imperative to develop strategies to enhance light utilization in TiO_2 photoelectrodes.

Band structure engineering is a widely used approach to enhance the electrical and optical properties of semiconductors. Among different band structure engineering approaches, point defect introduction is becoming increasingly important for improving and tailoring bulk semiconductors and their surfaces.[6,7] This approach has been shown to improve the solar light harvesting capability, charge separation, and charge transfer. For instance, oxygen vacancies (V_O) are shallow donors that increase the charge carrier concentration, resulting in improved performance.[8,9] Recently, TiO_2 with a continuous oxygen-vacancy gradient was reported to exhibit high light absorption and considerable photoelectrochemical performance improvement.[10] In addition to V_O, Ti vacancies (V_{Ti}) also play

M. Yang, J. Cui, M. Daboczi, A. Hankin, S. Eslava
Department of Chemical Engineering and Centre for Processable Electronics
Imperial College London
London SW7 2AZ, UK
E-mail: s.eslava@imperial.ac.uk
R. V. Law
Department of Chemistry
Imperial College London
White City Campus, London W12 0BZ, UK
J. Luke, J.-S. Kim
Department of Physics and Centre for Processable Electronics
Imperial College London
London SW7 2AZ, UK

The ORCID identification number(s) for the author(s) of this article can be found under https://doi.org/10.1002/admi.202300595

DOI: 10.1002/admi.202300595

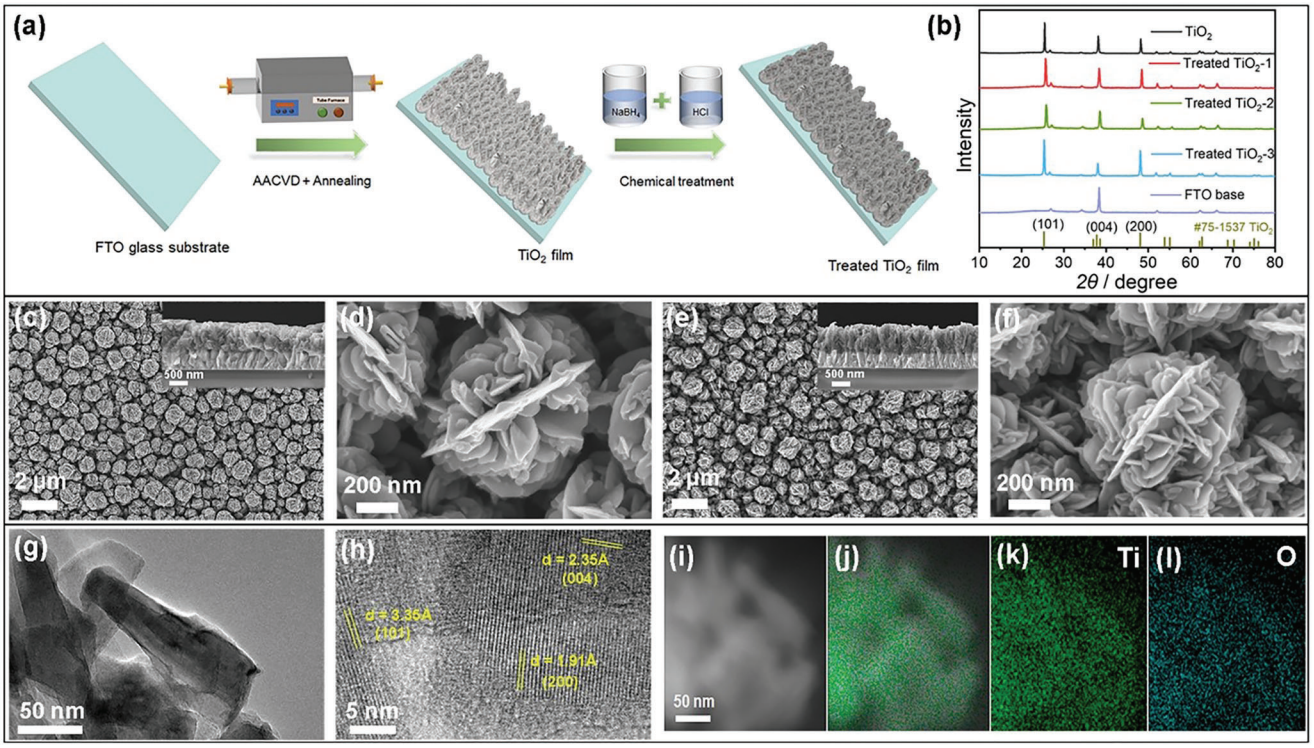

Figure 1. a) Schematic illustration of the synthesis of Treated TiO_2 samples. b) XRD patterns of TiO_2, Treated TiO_2-1, Treated TiO_2-2, and Treated TiO_2-3. c,d) SEM micrographs of pristine TiO_2 (inset: SEM cross-section image). e,f) SEM micrographs of Treated TiO_2-2 (inset: SEM cross-section image). g–i) TEM, HRTEM, and STEM micrographs of Treated TiO_2-2. j–l) EDX-mapping micrographs: j) overlap of Ti and O, k) Ti, and l) O.

a crucial role in improving the oxygen evolution reaction (OER) catalytic activity of TiO_2. However, the coexistence of V_O and V_{Ti} in TiO_2 has been rarely reported. This is because, in synthesized TiO_2 materials, V_O is responsible for intrinsic n-type conductivity and V_{Ti} for intrinsic p-type conductivity. It is challenging to simultaneously observe atomic-/nano-scaled V_{Ti} in the macro-scaled O-vacancy phases.[11]

Herein, we report on the successful introduction of different point defects, namely V_O and V_{Ti}, in TiO_2 photoanodes through a chemical treatment process at room temperature, utilizing $NaBH_4$ as a reductant, followed by HCl washing. A range of advanced techniques were employed to investigate the intrinsic band energy structure of the synthesized TiO_2 photoanodes. The results of ex situ and in situ characterization reveal that the formation of V_O and V_{Ti} can result in favorable effects on photoanodes, leading to an enhancement in the PEC performance. The enhanced PEC performance was attributed to the interplay of collective and localized effects of point defects on TiO_2. For the collective effects, we found that the increased point defects could lead to increased light absorption, enhanced donor density, conductivity and photovoltage, as well as a more negative flat-band potential. Additionally, our results show that the presence of localized surface V_{Ti} surrounded by O^- can increase the amount of surface hydroxyls and create a more basic environment for Ti—OH species. This, in turn, facilitates the water oxidation process by serving as trapping sites and self-reduction sites during OER. Overall, our findings shed light on the role of point defects in the water oxidation process on anatase TiO_2 and provide valuable insights into the development of high-performance photoanodes for sustainable energy conversion applications.

2. Results and Discussion

2.1. Structural Characterization

TiO_2 photoanodes were synthesized through aerosol-assisted chemical vapor deposition (AACVD) at 450 °C using toluene solutions of $Ti_7O_4(OEt)_{20}$ precursor, nitrogen gas carrier, and fluorine-doped tin oxide (FTO) coated aluminoborosilicate glass substrate.[5] After the synthesis, the photoanodes were annealed in air at 800 °C to remove carbon residues and achieve optimal TiO_2 crystallization. Some of these photoanodes were subsequently treated using 0.1, 0.2, or 0.3 M $NaBH_4$ ethanolic solutions and 1 M HCl aqueous solution and named Treated TiO_2-1, −2, or −3, respectively (**Figure 1**a). The phase of the synthesized photoanodes was characterized by measuring XRD diffractograms of obtained samples before and after chemical treatment. The peaks in the XRD diffractograms at 2θ of 25.5, 37.9, and 47.9° correspond to (101), (004), and (200), respectively, indicating that the TiO_2 films are the anatase crystalline phase (Figure 1b; Figure S1, Supporting Information). The morphology of the resulting films was inspected using scanning electron microscopy (SEM). The SEM micrographs show a homogeneous coverage of TiO_2 on the FTO layer for both pristine TiO_2 and treated TiO_2 photoanodes in Figure 1c–f and Figures S2 and S3 (Supporting Information). The thickness of the TiO_2 films is ≈1.5 μm (Figure 2c,e

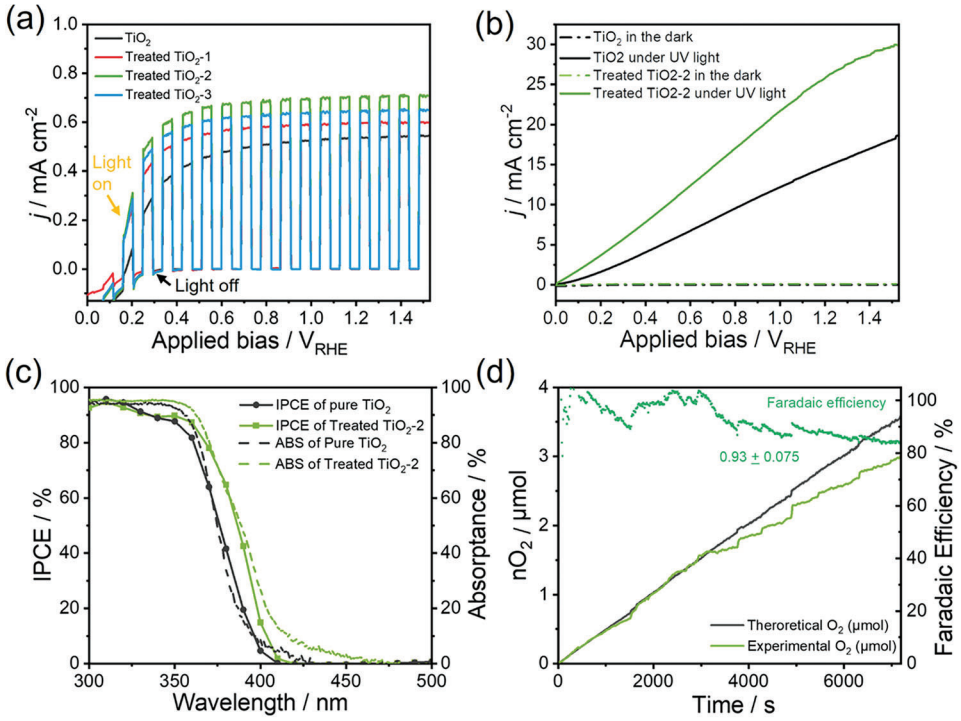

Figure 2. a) Current–voltage curves of TiO_2 and Treated TiO_2 photoanodes under 1 sun (Xe source, AM 1.5G filter, 100 mW cm^{-2}) chopped illumination at a scan rate of 10 mV s^{-1}. b) Current–voltage curves of photoanodes under UV light of 365 nm (100 mW cm^{-2}) and in the dark. c) IPCE spectra (solid line, left) at 1.23 V_{RHE} and UV–vis absorptance (dash line, right). d) Amount of measured and theoretical oxygen evolution and calculated Faradaic efficiency of Treated TiO_2-2 at an applied bias of 1.23 V_{RHE}. All these measurements were carried out in 1 M NaOH aqueous solution.

inset), and the morphology was preserved after additional chemical treatment. TiO_2 grains are grown on the FTO with a good coalescence and top layers are aggregations, clusters of perpendicular faceted grains, similar to so-called "desert roses" of gypsum or baryte. Transmission electron microscope (TEM) micrographs on a scraped piece of treated TiO_2 sample show TiO_2 grains of plate shape with lengths of ≈150 nm (Figure 1g) and thicknesses of ≈10 nm (Figure 2f). The high-resolution TEM (HRTEM) micrograph in Figure 1h shows stacked grains and lattice fringes with interplanar distances of 3.35, 2.35, and 1.91 Å that are indexed to (101), (004), and (200) planes of TiO_2, respectively. A scanning TEM (STEM) micrograph of Treated TiO_2-2 and its corresponding energy dispersive X-ray spectroscopy (EDX) elemental mapping micrographs show a uniform distribution of Ti and O elements with no other elements present (Figure 1i–l). Overall, the results indicate that the synthesized TiO_2 photoanodes have a well-defined morphology and crystalline structure.

2.2. Photoelectrochemical Characterization

The performance of TiO_2 photoanodes was evaluated using various PEC techniques. **Figure 2**a shows the current-voltage curves under chopped simulated sunlight (1 sun, 100 mW cm^{-2}) in 1 M NaOH aqueous solution (pH 13.7). All the TiO_2 photoanodes exhibited positive photocurrents during anodic sweeps at a scan rate of 10 mV s^{-1}, with an onset potential around 0 V_{RHE}. The treated TiO_2 photoanodes showed higher photocurrents, with the optimal results achieved for Treated TiO_2-2 sample. The current-voltage results for three series of samples were obtained, confirming reproducibility (Figure S4, Supporting Information). The optimal Treated TiO_2-2 photoanode showed a photocurrent of 0.54 (± 0.027) mA cm^{-2} at +0.34 V_{RHE} and 0.73 (± 0.015) mA cm^{-2} at +1.23 V_{RHE}, compared with 0.34 (± 0.044) mA cm^{-2} at +0.34 V_{RHE} and 0.53 (± 0.015) mA cm^{-2} at +1.23 V_{RHE} for pristine TiO_2 photoanode. Moreover, the photocurrent of Treated TiO_2-2 photoanode under UV light (365 nm, 100 mW cm^{-2}) was 26.4 mA cm^{-2} at +1.23 V_{RHE} as shown in Figure 2b, which was much higher than that of pristine TiO_2 (14.9 mA cm^{-2} at +1.23 V_{RHE}). Control tests were conducted on samples treated with 0.2 M $NaBH_4$ ethanolic solution and with only 1 M HCl at room temperature (Figure S5, Supporting Information). After only $NaBH_4$ treatment, the photocurrent of the sample increased from 0.53 mA cm^{-2} to 0.67 mA cm^{-2} at +1.23 V_{RHE}, which was higher than that of pristine TiO_2 but slightly less than that of fully Treated TiO_2-2 (0.73 mA cm^{-2} at +1.23 V_{RHE}). The limited improvement might be caused by the presence of coated by-products during the treatment, such as B_2O_3 or other boron oxide species, which are only washed away upon HCl acid wash.[12] On the other hand, after only HCl washing, the photocurrent plateau did not change, but slightly larger photocurrents were achieved at applied potentials below +0.6 V_{RHE} (Figure S5a, Supporting Information). The photocurrent analysis confirmed that Treated TiO_2-2 had the best PEC performance. Therefore, we focused our subsequent characterization efforts on this sample and pristine TiO_2 for comparison.

To characterize the translation of light absorption to final PEC performance, we conducted measurements of ultraviolet-visible

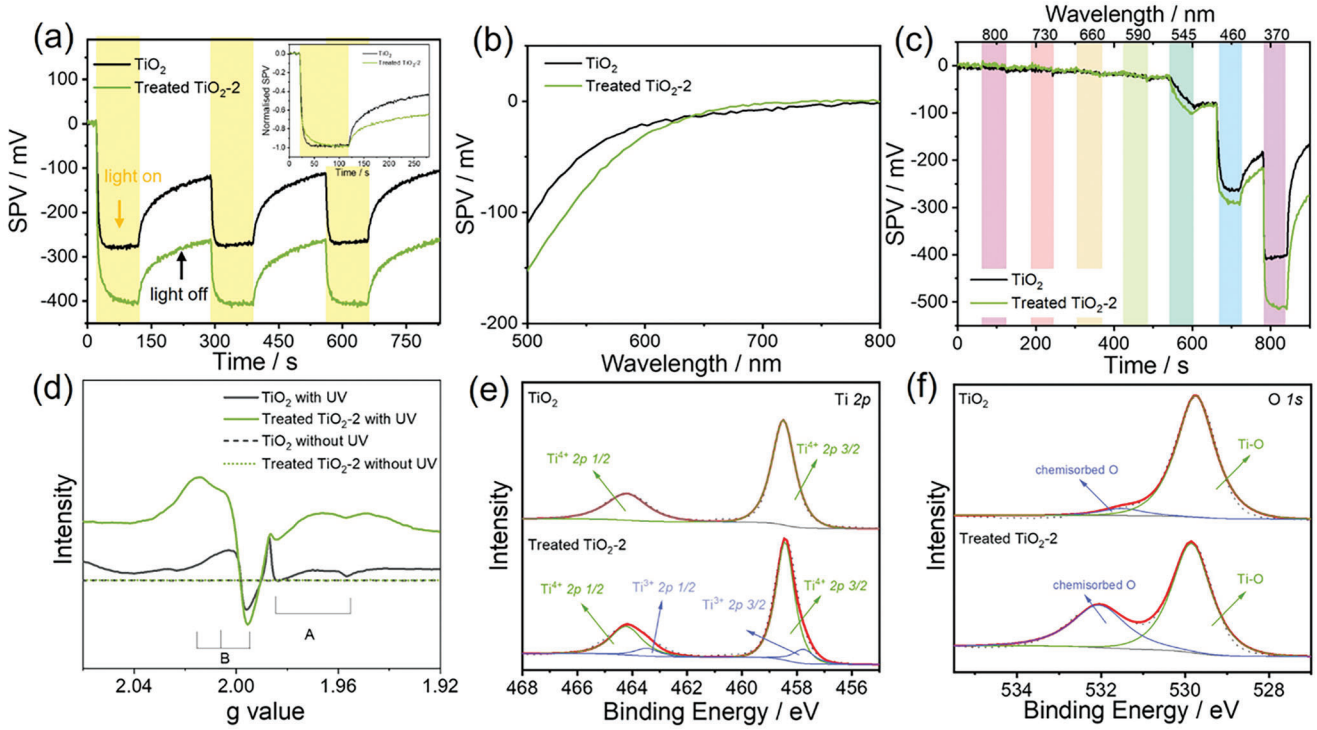

Figure 3. a) Surface photovoltage (SPV) signals of TiO_2 and Treated TiO_2-2 with white light illumination (20 mW cm^{-2}). Inset: normalized SPV rise and decay curves. b) SPV spectra recorded in the wavelength range of 500–800 nm with 5 nm step size. c) SPV signals with monochromatic LED illumination with wavelengths between 370 and 800 nm. d) EPR spectra at low temperature (4.2 K) under UV light of 360 nm and in the dark. e) High-resolution Ti *2p* XPS spectra and f) O *1s* XPS spectra.

(UV–vis) spectroscopy and IPCE for both pristine and treated TiO_2 photoanodes. As shown in Figure 2c, both samples exhibit an absorption edge corresponding to the bandgap of anatase TiO_2 of 3.2 eV. However, the absorptance of the Treated TiO_2-2 sample is slightly red-shifted by 10–20 nm, indicating a greater ability to absorb the solar spectrum. Similarly, the IPCE curves show an IPCE edge assigned to the bandgap of anatase TiO_2, with IPCE values approaching 100% in the UV range. The Treated TiO_2-2 sample also exhibits a red-shifted IPCE, achieving higher values than the pristine TiO_2 sample over a broader range. This red-shifted IPCE provide evidence for the treated photoanodes absorbing and converting more UV and violet light into photocurrent. To confirm that the enhanced photocurrents observed in the treated samples result in oxygen evolution reaction (OER), we conducted experiments using a gas-tight PEC cell at 1.23 V_{RHE} for 2 h, measuring the O_2 content inside the cell with a fiber-optic oxygen meter (Figure 2d). The results indicate that the Faradaic efficiency for OER was practically 100% for the first hour and 85–90% for the second hour. We attribute the decrease in Faradaic efficiency during the second hour to diffusion or small leakage of O_2 through rubber fittings, O_2 reduction in the counter electrode, or bubble trapping at the reactor walls, resulting in a reduced O_2 amount detected by the sensor. The high Faradaic efficiency of the Treated TiO_2-2 photoanodes confirms that the increased photocurrent results from water oxidation rather than oxidation of the TiO_2 materials. To test the stability of the samples, we conducted photocurrent measurements for 40 h under continuous simulated sunlight and 1.23 V_{RHE} with a 30-min dark interval halfway through the experiment (Figure S6, Supporting Information). After 20 h, the Treated TiO_2-2 sample retained 79% of its initial photocurrent, with half of the loss attributed to bubble formation on the photoanode surface and consequent blockage of the electroactive surface area. During the 30-min dark interval, we removed the bubbles by means of electrode agitation, and the photocurrent recovered 90% of its initial value. The final photocurrent after the 40-hour stability test was 76% of its initial value, indicating reasonable stability of the sample.

2.3. Energetics and Defect States of TiO_2

To understand the origin of improved PEC performance, we investigated the energy levels and in particular the defect states of the treated and pristine TiO_2. Surface photovoltage (SPV) signals were recorded for pristine TiO_2 and Treated TiO_2-2 by measuring the surface potential in the dark (WF_{dark}) and under illumination (WF_{light}). The magnitude and sign of SPV is defined here as the change in surface potential: $SPV = WF_{light} - WF_{dark}$. The negative sign of SPV under white light illumination (**Figure 3**a) is consistent with an increased density of holes at the surface of the n-type TiO_2, which could result from photoexcitation of electrons from both the valence band as well as electronic trap states within the bandgap, as shown in Figure S7 (Supporting Information).[13,14] The larger SPV magnitude and the slower SPV rise/decay (i.e., slower trapping/de-trapping) under white light illumination suggest the presence of higher density of electronic trap states in the

Treated TiO_2-2 compared to TiO_2. SPV spectra using a monochromator in Figure 3b show significant magnitude of SPV even under sub-bandgap illumination (i.e., lower energy compared to the bandgap of 3.2 eV), providing evidence for trap states filled with electrons within the bandgap of TiO_2. Importantly, the larger magnitude of sub-bandgap SPV signal and a clear redshift (from 550 to 600 nm) in the SPV onset for the Treated TiO_2-2 compared to the reference TiO_2 confirm an increased density of trap states 2.1 eV (600 nm illumination) below E_c. We assign these to Ti vacancies (V_{Ti}) in the TiO_2 crystal structure, which were calculated to be also at 2.1 eV below E_c.[15] Similar trap states related SPV signals were also recorded at lower light intensities using different monochromatic LEDs of wavelengths between 800 and 370 nm (Figure 3c).

To gain further understanding of the trap states present in the samples, EPR spectra were recorded under low temperature and with/without UV light illumination, which are depicted in Figure 3d. We compared the *g* values of TiO_2 and Treated TiO_2-2, which are highly dependent on the crystallographic geometry of compounds and other magnetic couplings such as spin-orbit.[16] Compared with the EPR data with/without UV illumination, the EPR spectra with UV illumination of TiO_2 and Treated-TiO_2-2 exhibit two sets of signals, denoted as *A* and *B*, which arise from electrons and holes, respectively. The sharp signal observed at g_{A1} = 1.987 and g_{A2} = 1.956 is attributed to electron trapping sites, indicating the presence of Ti^{3+} in solid TiO_2 samples. The EPR signals with *g* factors g_{B1} = 2.014, g_{B2} = 2.003 and g_{B3} = 1.996 correspond to hole trapping sites, which are assigned to O^- stabilized by surface hydroxyls in solid TiO_2 samples.[17,18] O^- radicals are generated by photogenerated holes that are trapped by low-coordinate bridging O^{2-} anions or pre-existing O^-. Upon chemical treatment, the Treated TiO_2-2 sample exhibits increased signal intensities for both A and B, indicating an increase in the amounts of Ti^{3+} and O^- species. These species have the capability to compensate for O^{2-} deficiencies (V_O) and Ti deficiencies (V_{Ti}) resulting from the chemical treatment.

To investigate the composition and surface chemical environment of TiO_2 and Treated TiO_2 samples, X-ray photoelectron spectroscopy (XPS) analysis was carried out. The survey XPS spectra in Figure S8 (Supporting Information) reveal that both TiO_2 and Treated TiO_2-2 consisted of the same elements, including Ti, O and adventitious C. The high-resolution XPS spectra of Ti *2p* and O *1s* regions of samples are presented in Figure 3e,f. The Ti *2p* spectrum of TiO_2 showed peaks at 464.2 and 458.5 eV in Ti^{4+} state, corresponding to Ti *2p1/2* and *2p3/2*, respectively. In contrast, the Ti *2p* spectrum in Treated TiO_2 samples (in the Ti^{4+} state) showed a small shift to lower binding energy, and peaks of Ti^{3+} were observed at 463.2 and 457.5 eV, which is assigned to the reducing effect of $NaBH_4$.[19] The O *1s* XPS spectra were identified via two peaks in Figure 3f. The peak at 529.8 eV was allocated to lattice oxygen (Ti-O band), where a small shift to lower binding energy occurred in Treated TiO_2 samples, indicating lower Ti coordination due to the increased amount of V_O in TiO_2 as shown in EPR results. The other peak is associated with chemisorbed O, of which the intensity increased significantly in Treated TiO_2-2 after chemical treatment. The formation of O *1s* peak about 529–532 eV is quite complex and can be deconvoluted to different oxygen species. According to previous studies, this peak could be allocated to hydroxy species of surface-adsorbed water molecules (~532 eV) and defect sites with low oxygen coordination (~531 eV).[20] The defect sites with low oxygen coordination includes V_O and O^-, which correlate with Ti^{3+} and the V_{Ti} compensating for the Ti^{4+} deficiencies, respectively.[21],[22] Therefore, the increased peak intensity (529-532 eV) can be attributed to the influence of these increased oxygen species simultaneously.

The valence band density of states (DOS) of TiO_2 and Treated TiO_2-2 were also measured using valence band XPS and are presented in **Figure 4**a. The valence band DOS of pristine TiO_2 exhibited typical characteristics of TiO_2, with the valence band edge (E_V) 2.85 eV below the Fermi level. In contrast, the E_V of Treated TiO_2-2 was 0.12 eV shifted to lower binding energy, which is attributed to the increased amount of V_{Ti}. These observations are consistent with the SPV results, indicating the introduction of V_{Ti} in the sample after chemical treatment.

Work function measurements show that the Fermi level of the Treated TiO_2-2 (–4.40 eV) is shallower than of the pristine TiO_2 (−4.66 eV) (Figure 4b). The optical bandgap values of TiO_2 and Treated TiO_2-2 (Figure S9d, Supporting Information) and the E_V values allow the calculation of the E_C values at –4.18 and –3.98 eV, respectively. These energy levels confirm a stronger n-type characteristic of the Treated TiO_2-2, which is typically related to the V_O acting as electron donors.[23] Consequently, the shallower Fermi level of the Treated TiO_2-2 can be linked to an increased density of V_O, which is in good agreement with the XPS and EPR results.

2.4. Mechanism of Point Defect Formation

Based on the analysis conducted above, a higher concentration of Ti^{3+} and O^- was observed in Treated TiO_2 samples. In this section, we propose a possible mechanism for the formation of these point defects in TiO_2. During the chemical treatment process, Ti^{4+} underwent reduction to Ti^{3+} along with oxygen-vacancy sites [$V_O^{\bullet}Ti^{3+}$], while V_{Ti} was produced along with O^- pieces [$V_{Ti}^{\bullet}O^-$] due to the O-rich microenvironment formed by the escaping oxygen from V_O.[11]

Initially, Ti^{4+} could be reduced to Ti^{3+} by $NaBH_4$, following the reaction

$$8Ti^{4+} + NaBH_4 + 2H_2O \rightarrow 8Ti^{3+} + NaBO_2 + 8H^+ \quad (1)$$

along with the generation of oxygen vacancy sites [$V_O^{\bullet}Ti^{3+}$].[12] The formation of V_O and V_{Ti} can be demonstrated using the reaction equations using Kröger–Vink notation:[11,16,24]

$$V_O \text{ formation}: \quad O_O \rightarrow V_O^{\bullet\bullet} + 2e + 1/2\,O_2 \quad (2)$$

$$O_O \rightarrow V_O^{\bullet\bullet} + 2e' + O_E^x \quad (3)$$

$$Ti^{3+} \text{formation}: \; Ti_{Ti} + e' \rightarrow Ti_{Ti}' \quad (4)$$

$$V_{Ti} \text{ formation}: \quad 2O_E^x \rightarrow V_{Ti}'''' + 4h^{\bullet} + 2O_O \quad (5)$$

$$O^- \text{ formation}: \quad h^{\bullet} + O_O \rightarrow O_O^{\bullet} \quad (6)$$

where O_O represents lattice oxygen, Ti_{Ti} lattice titanium, $V_O^{\bullet\bullet}$ oxygen vacancy, V_{Ti}'''' titanium vacancy, e′ represents electron, $h^{\bullet}$

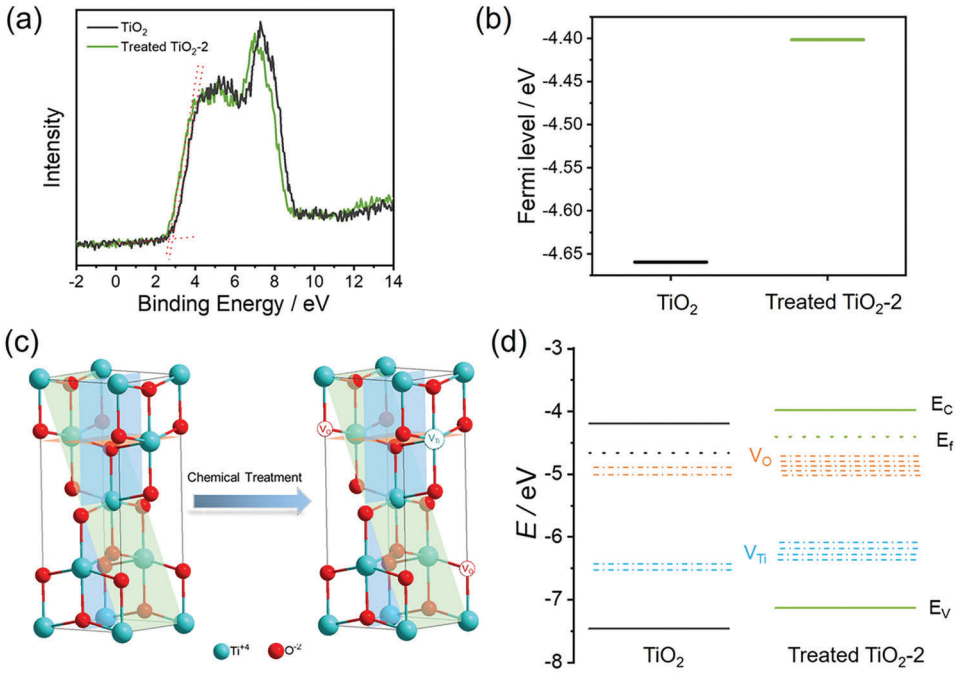

Figure 4. a) Density of states of the valence band of TiO_2 and Treated TiO_2-2. b) Fermi level energy of TiO_2 and Treated TiO_2-2 calculated from the contact potential difference (CPD) between tip and samples. c) Atomic structure diagram before and after chemical treatment. d) Schematic energy diagram of TiO_2 and Treated TiO_2-2.

represents hole, $O_O^{\bullet}$ represents O^-, and O_E^x represents escaping oxygen of dynamic state/balance.

The atomic structure diagram of TiO_2 and Treated TiO_2-2 samples are presented in Figure 4c. Unlike TiO_2, Treated TiO_2-2 exhibits point defects, including V_O and V_{Ti}, which were introduced via chemical treatment. Based on this, we propose the energy diagram in Figure 4d. The introduction of V_{Ti} in Treated TiO_2-2 results in a higher E_V, while V_O causes a higher Fermi level and smaller energy bandgap.

2.5. Effects of the Point Defects

The influence of point defects on light absorption was examined using UV–vis spectroscopy measurements for TiO_2 and Treated TiO_2-2, which are shown in Figure S9 (Supporting Information). To exclude the influence of acid wash on light absorption, the UV–vis absorbance spectrum of TiO_2 washed by HCl was also measured (Figure S9b, Supporting Information), indicating that acid wash did not affect the light absorption of TiO_2 samples. Compared to TiO_2, a shift in the reflectance curve edge toward higher wavelengths was observed after chemical treatment, indicating higher light absorption in Treated TiO_2-2. The Kubelka-Munk function of optical reflectance curves for pristine TiO_2 and Treated TiO_2-2 in Figure S9d (Supporting Information) reveals that the bandgap of pristine TiO_2 and Treated TiO_2-2 is ≈3.27 and 3.19 eV, respectively. Band tail states were also observed after chemical treatment. The decreased bandgap and band tail states as well as the increased light absorption after chemical treatment are assigned to the increased presence of point defects, which is consistent with the SPV and EPR results.

To further investigate the bulk and surface properties of the photoanodes, we conducted electrochemical impedance spectroscopy (EIS) measurements in the dark. The obtained EIS data are presented in the form of Mott–Schottky (M–S) plots at 500, 1000, and 2000 Hz, as illustrated in Figure S10 (Supporting Information). The frequency dispersion of the Mott-Schottky plots originates from current and potential distributions due to interface inhomogeneities, which might be attributed to surface disorder, roughness, and electrode porosity.[25] The M–S plots revealed that the synthesized photoanodes exhibited a positive slope, which is a typical characteristic of n-type semiconductors. To determine flat-band potential (E_{fb}), we analyzed the M–S relationship by considering the capacitance of the space charge layer (C_{sc}) of the semiconductor electrode.[26] The E_{fb} values observed in Figure S10c (Supporting Information) exhibited a small variation of only 0.04 V between different frequencies, indicating a reasonable level of accuracy in the measured values for E_{fb}. The E_{fb} was estimated to be +0.19 and +0.14 V_{RHE} for pristine TiO_2 and Treated TiO_2-2, respectively, which is consistent with previous energy level measurements (Figure 4). Theoretically the E_{fb} of photoanodes in a certain electrolyte is dependent on the bulk Fermi level of the semiconductor and the potential drop of Helmholtz layer. The doping concentration affects the bulk Fermi level of the semiconductor, while surface conditions influence the potential drop of the Helmholtz layer. Therefore, the decrease in E_{fb} observed after chemical treatment may be attributed to an increase in donor density caused by point defects in the photoanodes. Additionally, the smaller slope values of M–S from Treated TiO_2-2 indicate an increased donor density, which promotes band bending and facilitate charge transport and charge injection,[27] consistent with the enhanced SPV intensity after

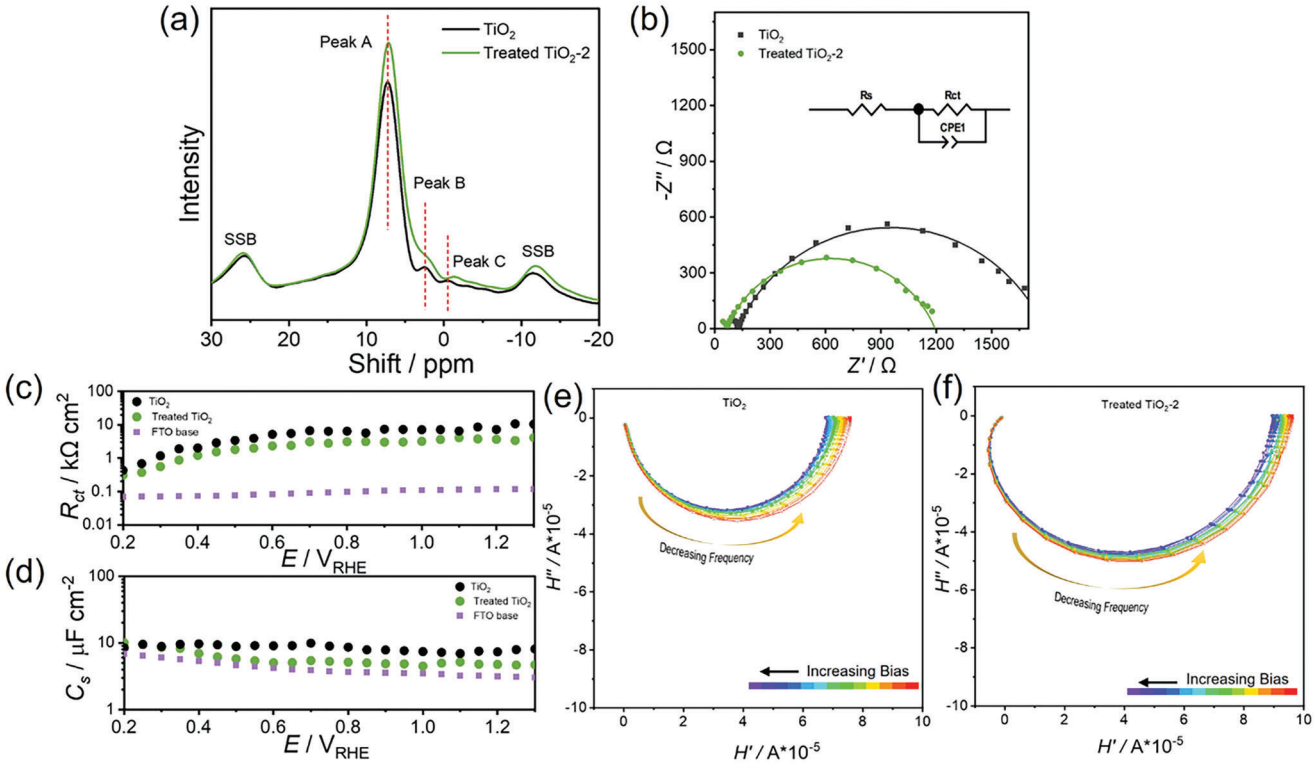

Figure 5. a) ^{1}H MAS-NMR spectra of TiO_2 and Treated TiO_2-2 at room temperature. b) Equivalent circuit and Nyquist plots at +0.83 V_{RHE} in 1 M NaOH solution with pH 13.7 under simulated sunlight (Xe source, AM 1.5G, 100 mW cm^{-2}). c,d) R_{ct} and C_s as a function of applied bias between +0.20 and +1.3 V_{RHE} in 1 M NaOH solution with pH 13.7 under simulated sunlight. e,f) IMPS spectra as a function of applied bias between +0.1 and +1.3 V_{RHE} in 1 M NaOH solution under 365 nm LED (illumination (37.5 mW cm^{-2}) with a modulation of 50% in light intensity, over a frequency range from 10^3 to 0.1 Hz at each potential step.

chemical treatment, as well as the observed higher PEC photocurrent and higher IPCE efficiency.

To further explore the influence of chemical treatment on the photoanode performance, the contact angles of pristine TiO_2 and Treated TiO_2-2 with water were also measured and presented in Figure S11 (Supporting Information). The contact angle of Treated TiO_2-2 was found to be much smaller than that of pristine TiO_2 (10° vs 40°), indicating that the surface of Treated TiO_2-2 with its higher presence of point defects is more hydrophilic. A more hydrophilic photoanode surface is expected to improve the first OER steps of hydroxyl adsorption, thereby improving photoanode currents. To better understand the effects of the chemical treatment, proton magic angle spinning nuclear magnetic resonance (^{1}H MAS NMR) spectra of the samples were collected. The results of ^{1}H MAS NMR are shown in **Figure 5**a. Two peaks, symmetrical about the centre, at 25.9 and –11.7 ppm could be observed, which are spinning side bands (SSB) that arise due to incomplete averaging of the homonuclear dipole-dipole interaction which predominates in ^{1}H NMR spectra. Both samples were evacuated to remove excess water. The pristine TiO_2 and Treated TiO_2-2 samples show an intense peak ≈7.2 ppm (peak A) and two lower intensity peaks at 2.6 ppm (peak B) and –0.6 ppm (peak C), indicating that there are at least three different types of chemical shift site for protons. The intense peak A is assigned to protons of residual adsorbed water. The linewidth of peak A is dominated by water mobility effects.[28] It is slightly narrower in pristine TiO_2 than Treated TiO_2-2. For Treated TiO_2-2, peak A is wider and increased in intensity, due to the more strongly adsorbed water protons of Treated TiO_2-2. This may be due to the increased number of potential hydrogen bonding sites present in Treated TiO_2-2. Peak B and C originate from hydroxyl protons (Ti—OH), with peak C being assigned to a more basic-type chemical environment.[29] For peak B, the major change is in both the peak shape, the intensity and a slight shift toward the right-hand side of the spectrum, as it is now much broader than the pristine TiO_2 peak. The increase in intensity is due to the higher concentration of hydroxyl groups of Treated TiO_2-2 compared to pristine TiO_2 and may indicate a higher concentration of oxygen deficiencies where adsorbed water can be dissociated.[30] The increase in basic character of the Ti-OH, for both peak B and C, causes a movement toward the right-hand side of the spectrum.[28] In Treated TiO_2-2, this indicates that part of absorbed groups is more basic (more shielded). This agrees with the analysis of SPV, EPR, and XPS, where it was observed that there was an increase in the concentration of O^- species, which in turn generated a more basic environment. It has been demonstrated that hydroxyls on a catalyst surface can significantly enhance its catalytic activity.[31] First, they can act as trapping sites, facilitating rapid proton exchange between the defect-involved bridging hydroxyl groups and the adsorbed molecules.[32] Second, the self-reduction of surface hydroxyl into water can significantly reduce the overpotential for OER, thereby boosting the OER activity of catalyst.[33]

Therefore, the improved PEC performance of Treated TiO_2-2 may also be attributed to the increased water adsorption and hydroxyls on the surface after chemical treatment.

Open circuit potential (OCP) measurements were also conducted to further research and compare the PEC response of these TiO_2 samples. Figure S12a,b (Supporting Information) shows the OCP curves for both pristine TiO_2 and Treated TiO_2-2 photoanodes measured under intermittent visible light at different light intensities, with the OCP response to illumination shifting to smaller potential. The initial negative shift in OCP was due to the transfer of the excited photoelectrons from the bulk to the surface.[34] The relatively stable OCP values observed thereafter can be attributed to the balance between the generation and recombination of photoexcited electrons.[35] Upon switching off the irradiation, the OCP values for Treated TiO_2-2 were observed to return to their original values at a slower speed compared to TiO_2. This phenomenon may be due to the electron pool effect of Treated TiO_2-2, which is enhanced by a higher donor intensity after chemical treatment. The electron pool effect allows for the storage of photoinduced electrons under light irradiation and their slow release in the absence of light. Figure S12c (Supporting Information) displays the OCP values of both pristine TiO_2 and Treated TiO_2-2 photoanodes, with the latter exhibiting a higher donor intensity following chemical treatment. Additionally, the illuminated OCP can be utilized to estimate the E_{fb} when the illumination intensity exceeds 300 mW cm^{-2}, which is sufficiently intense to fully eliminate pre-existing band bending at the surface.[26,36] Under light irradiation, the OCP value for TiO_2 was approximately +0.14 V_{RHE}, while the OCP values for Treated TiO_2-2 reached +0.12 V_{RHE}, indicating that Treated TiO_2-2 photoanode has a smaller E_{fb} and exhibits the same trend as the M–S measurement results. The photovoltages (V_{ph}) of the TiO_2 and Treated TiO_2-2 photoanodes were calculated and presented in Figure S12d (Supporting Information). The Treated TiO_2-2 photoanode possesses a higher V_{ph} value than pristine TiO_2, indicating a greater driving force for the OER reaction and higher internal electric fields that can minimize charge recombination.

2.6. OER Kinetics

To characterize the OER kinetics of these photoanodes, we used photoelectrochemical impedance spectroscopy (PEIS) and intensity modulated photocurrent spectroscopy (IMPS). PEIS is a powerful method for analyzing charge transfer and recombination processes at semiconductor-electrolyte interfaces, and we conducted it at various applied biases. Figure 5b shows typical Nyquist plots with the equivalent circuit obtained in 1.0 M NaOH aqueous solution for the illuminated photoanodes. The equivalent circuit includes two resistances, one attributed to the electrolyte and conductive substrate layer (R_s), and the other attributed to the TiO_2-electrolyte junction (R_{ct}). A constant phase element (CPE) was applied to account for the distribution of the time constants in porous and defective photoanodes.[21] The R_{ct} values as a function of applied bias are shown in Figure 5c. The R_{ct} values of the treated TiO_2 photoanodes were smaller than those of pristine TiO_2, indicating a more effective separation and easier charge transfer of photogenerated electron-hole pairs across the TiO_2-electrolyte junction. The results show that the introduced point defects must serve as intermediate surface states (i-ss) on photoanodes, facilitating the interfacial charge transfer process. Capacitance (C_s) values were calculated from CPE values and shown in Figure 5d. The C_s in treated TiO_2-2 was close to pristine TiO_2, and the slightly smaller C_s might be attributed to the occupied surface states by absorbed water and hydroxyls. To exclude the influence on the behavior of R_{ct} and *Cs* of the FTO base on the results, the R_{ct} and C_s values of a bare FTO base were measured and added to Figure 5c,d. The *Rct* and C_s values were much smaller than those of TiO_2 and Treated TiO_2-2 samples, showing the small influence of FTO on the measurement. The R_{ct} and C_s values of the FTO base, TiO_2 and Treated TiO_2 samples were also calculated at +0.83 V_{RHE} under both light and dark in 1 M NaOH, as shown in Figure S13 (Supporting Information). The results show that the R_{ct} and C_s values of the FTO base did not change with/without light and were lower than the TiO_2 samples, which also shows that the behavior of extracted capacitance is from TiO_2 samples rather than FTO base. In addition, electrochemically active surface area (ECSA) measurements and corresponding CV curves are shown in Figure S14 (Supporting Information). In such measurements, the slope of the current density versus scan rate can be related to the double layer capacitance (C_{dl}), which is directly proportional to the ECSA. Based on the obtained results, Treated TiO_2-2 possesses a slightly higher surface area (C_{dl} = 0.037 mF cm^{-2}) than pristine TiO_2 (C_{dl} = 0.028 mF cm^{-2}), suggesting that the chemical treatment has a small influence on the surface morphology of TiO_2. This finding contrasts with the smaller C_s values obtained on Treated TiO_2-2 via PEIS, which can be attributed to the fact that the ECSA measurements were performed in the dark, whereas the PEIS measurements were conducted under light illumination. We attribute the slightly smaller C*s* value of Treated TiO_2-2 to the presence of occupied surface states resulting from an increased number of potential hydrogen and hydroxyl bonding sites under light illumination. IMPS was conducted to investigate the reaction kinetics on pristine TiO_2 and treated TiO_2-2 photoanodes. Similar to PEIS plots, depressed semicircles were observed owing to distributed time constants. Typically, the IMPS spectrum for an n-type photoanode consists of two semicircles located in the first and fourth quadrant.[37] The high frequency semicircle starts in the fourth quadrant, representing the attenuation by the total resistance of the cell and combined space charge capacitance and Helmholtz layer capacitance. By decreasing the frequency of perturbation surface recombination and charge transfer processes dominate, giving another semicircle in the first quadrant.[38,39] In Figure 5e,f, only semicircles in the fourth quadrant are observed in the entire applied bias range. This suggests negligible surface recombination on pristine TiO_2 and Treated TiO_2-2 photoanodes, which is consistent with the high IPCE values. The high frequency intercept point of Treated TiO_2-2 is notably higher than that of the TiO_2 sample, indicating a higher hole flux at the surface, consistent with the larger photovoltage in OCP measurements (Figure S12d, Supporting Information).

We propose a mechanism to explain the enhanced PEC performance upon chemical treatment with $NaBH_4$ and HCl wash. The efficiency of a photoanode can be evaluated by considering the following three consecutive steps: light absorption (η_{abs}), separation of electrons and holes to the current collector and electrode

surface, respectively, (η_{sep}), and gas evolution reaction (η_{rxn}), as shown in Equation (7).[40]

$$\eta_{cell} = \eta_{abs} \times \eta_{sep} \times \eta_{rxn} \quad (7)$$

First, the presence of point defects in TiO_2 narrows the bandgap and improves η_{abs}. Second, the introduction of point defects increases the donor density of TiO_2, which enhances band bending and facilitates charge transport and charge injection, leading to improved η_{sep}. Additionally, the chemical treatment process results in the formation of V_{Ti} due to the O-rich microenvironment created by the oxygen escaping from V_O. The presence of surface V_{Ti} surrounded by O^- can enhance the number of hydroxyls on the surface, leading to the production of a more basic environment for Ti—OH. The increased hydroxyl density, in turn, facilitates the water oxidation process because they are adsorption sites and intermediates for OER,[32,33] ultimately improving the reaction efficiency η_{rxn}. Thus, due to the interplay of collective and localized effects of point defects, the PEC performance of TiO_2 is enhanced upon chemical treatment.

3. Conclusion

Our study has demonstrated the successful introduction of point defects (Vo and V_{Ti}) in AACVD nanostructured TiO_2 photoanodes through chemical treatment involving $NaBH_4$ and HCl. This treatment led to enhanced photoelectrochemical water oxidation in alkaline electrolyte. Treated TiO_2 photoanodes exhibited a photocurrent density of 0.54 mA cm^{-2} at +0.34 V_{RHE} and 0.73 mA cm^{-2} at +1.23 V_{RHE} with a high IPCE efficiency near 100%, surpassing the performance of pristine TiO_2. Various spectroscopic techniques confirm the introduction of point defects and the interplay of their collective and localized effects which lead to increased light absorption, donor density, conductivity and photovoltage, and reduced flat-band potential, as well as increased hole flux at the TiO_2 surface. Our findings demonstrate a straightforward pathway to introduce point defects on oxide semiconductor surfaces and emphasize their importance and complex role to advance photoelectrodes for solar fuel technologies.

Supporting Information

Supporting Information is available from the Wiley Online Library or from the author.

Acknowledgements

The authors thank the Department of Chemical Engineering at Imperial College London for the funding of a Ph.D. scholarship for M.Y. S.E. and M.D. thank the UK EPSRC grant EP/S030727/1 for financial support. J.L. and J.S.K. acknowledge the UK EPSRC for the ATIP PRogramme Grant (EP/T028513/1). The authors would like to acknowledge the UK EPSRC equipment funding for SPIN-Lab (EP/P030548/1).

Conflict of Interest

The authors declare no conflict of interest.

Data Availability Statement

The data that support the findings of this study are openly available in the Imperial College London research data repository at https://doi.org/10.14469/hpc/13251.

Keywords

charge separation efficiency, light absorption, photoelectrochemical water splitting, point defects, titanium dioxide photoanodes

Received: July 14, 2023
Revised: August 29, 2023
Published online: September 19, 2023

[1] Z. Liu, L. Wang, X. Yu, J. Zhang, R. Yang, X. Zhang, Y. Ji, M. Wu, L. Deng, L. Z. Li, L. Wang, *Adv. Funct. Mater.* **2019**, *29*, 1807279.
[2] K. Zhu, N. R. Neale, A. Miedaner, A. J. Frank, *Nano Lett.* **2007**, *7*, 69.
[3] L. Yu, Z. Wang, L. Shi, S. Yuan, Y. Zhao, J. Fang, W. Deng, *Appl. Catal. B.* **2012**, *113–114*, 318.
[4] Z. Ding, G. Q. Lu, P. F. Greenfield, *J. Phys. Chem. B.* **2000**, *104*, 4815.
[5] M. Regue, S. Sibby, I. Y. Ahmet, D. Friedrich, F. F. Abdi, A. L. Johnson, S. Eslava, *J. Mater. Chem. A.* **2019**, *7*, 19161.
[6] F. Wang, S. Yang, Q. Lu, W. Liu, P. Sun, Q. Wang, W. Cao, *Colloids Surf. A Physicochem. Eng. Asp.* **2023**, *658*, 130741.
[7] X. Wang, L. Mayrhofer, M. Keunecke, S. Estrade, L. Lopez-Conesa, M. Moseler, A. Waag, L. Schaefer, W. Shi, X. Meng, J. Chu, Z. Fan, H. Shen, *Small* **2022**, *18*, 2204136.
[8] Y. Yang, L.-C. Yin, Y. Gong, P. Niu, J.-Q. Wang, L. Gu, X. Chen, G. Liu, L. Wang, H.-M. Cheng, *Adv. Mater.* **2018**, *30*, 1704479.
[9] Y. Zhao, Y. Zhao, R. Shi, B. Wang, G. I. N. Waterhouse, L.-Z. Wu, C.-H. Tung, T. Zhang, *Adv. Mater.* **2019**, *31*, 1806482.
[10] K. H. Kim, C.-W. Choi, S. Choung, Y. Cho, S. Kim, C. Oh, K.-S. Lee, C.-L. Lee, K. Zhang, J. W. Han, S.-Y. Choi, J. H. Park, *Adv. Energy Mater.* **2022**, *12*, 2103495.
[11] S.-M. Wu, X.-L. Liu, X.-L. Lian, G. Tian, C. Janiak, Y.-X. Zhang, Y. Lu, H.-Z. Yu, J. Hu, H. Wei, H. Zhao, G.-G. Chang, G. Van Tendeloo, L.-Y. Wang, X.-Y. Yang, B.-L. Su, *Adv. Mater.* **2018**, *30*, 1802173.
[12] W. Fang, M. Xing, J. Zhang, *Appl. Catal. B-Environ.* **2014**, *160–161*, 240.
[13] M. Daboczi, I. Hamilton, S. Xu, J. Luke, S. Limbu, J. Lee, M. A. McLachlan, K. Lee, J. R. Durrant, I. D. Baikie, J.-S. Kim, *ACS Appl. Mater. Interfaces* **2019**, *11*, 46808.
[14] J. Luke, L. Corrêa, J. Rodrigues, J. Martins, M. Daboczi, D. Bagnis, J.-S. Kim, *Adv. Energy Mater.* **2021**, *11*, 2003405.
[15] M. Janczarek, E. Kowalska, *Catalysts* **2021**,*11*, 978.
[16] Q. Kang, J. Cao, Y. Zhang, L. Liu, H. Xu, J. Ye, *J. Mater. Chem. A.* **2013**, *1*, 5766.
[17] C. P. Kumar, N. O. Gopal, T. C. Wang, M.-S. Wong, S. C. Ke, *J. Phys. Chem. B.* **2006**, *110*, 5223.
[18] M. A. Henderson, *Langmuir* **1996**, *12*, 5093.
[19] Z. Gao, H. Yang, J. Mao, L. Kang, R. Zhang, S. Chai, J. Wu, W. Li, *Environ. Sci. Pollut. Res.* **2020**, *27*, 9748.
[20] Y. Lu, Y.-X. Liu, L. He, L.-Y. Wang, X.-L. Liu, J.-W. Liu, Y.-Z. Li, G. Tian, H. Zhao, X.-H. Yang, J. Liu, C. Janiak, S. Lenaerts, X.-Y. Yang, B.-L. Su, *Nanoscale* **2020**, *12*, 8364.
[21] J. Cui, M. Daboczi, M. Regue, Y.-C. Chin, K. Pagano, J. Zhang, M. A. Isaacs, G. Kerherve, A. Mornto, J. West, S. Gimenez, J.-S. Kim, S. Eslava, *Adv. Funct. Mater.* **2022**, *32*, 2207136.
[22] B. Zhang, L. Wang, Y. Zhang, Y. Ding, Y. Bi, *Angew. Chem., Int. Ed.* **2018**, *57*, 2248.
[23] W. P. Utomo, H. Wu, Y. H. Ng, *Small* **2022**, *18*, 2200996.

[24] L. Andronic, A. Enesca, *Front. Chem.* **2020**, *8*, 565489.
[25] P. Córdoba-Torres, T. J. Mesquita, O. Devos, B. Tribollet, V. Roche, R. P. Nogueira, *Electrochim. Acta* **2012**, *72*, 172.
[26] Z. Chen, H. Dinh, E. Miller, *Springer, Photoelectrochemical Water Splitting. Standards, Exprimental Methods, and Protocols*, Springer, New York, USA **2013**.
[27] X. Lv, L. Tao, M. Cao, X. Xiao, M. Wang, Y. Shen, *Nano Energy* **2018**, *44*, 411.
[28] J. Soria, J. Sanz, I. Sobrados, J. M. Coronado, M. D. Hernández-Alonso, F. Fresno, *J. Phys. Chem. C.* **2010**, *114*, 16534.
[29] J. Soria, J. Sanz, I. Sobrados, J. M. Coronado, F. Fresno, M. D. Hernández-Alonso, *Catal. Today.* **2007**, *129*, 240.
[30] M. A. Henderson, *Surf. Sci. Rep.* **2002**, *46*, 1.
[31] X. Xu, H. Liu, J. Wang, T. Chen, X. Ding, H. Chen, *Surf. Interfaces.* **2021**, *25*, 101272.
[32] Y. Zhao, T. Shi, J. Shang, L. Ding, X. Cao, C. Chen, J. Zhao, *Appl. Catal. B-Environ.* **2020**, *277*, 119234.
[33] Y. Zhao, J. Gu, Z. Chen, *Adv. Funct. Mater.* **2019**, *29*, 1904782.
[34] W. Wang, X. Wang, N. Wang, X. Ning, H. Li, D. Lu, X. Liu, Q. Zhang, Y. Huang, *Nanoscale Res. Lett.* **2018**, *13*, 295.
[35] M.-j. Zhou, Z.-o. Zeng, L. Zhong, *Corros. Sci.* **2009**, *51*, 1386.
[36] F. E. Bedoya-Lora, I. Holmes-Gentle, A. Hankin, *Curr. Opin. Green. Sust.* **2021**, *29*, 100463.
[37] F. E. Bedoya-Lora, M. E. Valencia-García, A. Hankin, D. Klotz, J. A. Calderón, *Electrochim. Acta.* **2022**, *402*, 139559.
[38] L. M. Peter, E. A. Ponomarev, D. J. Fermín, *J. Electroanal. Chem.* **1997**, *427*, 79.
[39] L. M. Peter, K. G. U. Wijayantha, A. A. Tahir, *Faraday Discuss.* **2012**, *155*, 309.
[40] J. Zhang, J. Cui, S. Eslava, *Adv. Energy Mater.* **2021**, *11*, 2003111.